Observations of the Antarctic Circumpolar Current Over the Udintsev Fracture Zone, the Narrowest Choke Point in the Southern Ocean

Young-Hyang Park, T. Park, T.-W. Kim, S.-H. Lee, C.-S. Hong, Jae Hak Lee, Marie-Hélène Rio, Marie-Isabelle Pujol, M. Ballarotta, Isabelle Durand, et al.

JGR Oceans

RESEARCH ARTICLE
10.1029/2019JC015024

Observations of the Antarctic Circumpolar Current Over the Udintsev Fracture Zone, the Narrowest Choke Point in the Southern Ocean

Y.-H. Park[1], T. Park[2], T.-W. Kim[2], S.-H. Lee[2], C.-S. Hong[3], J.-H. Lee[3], M.-H. Rio[4], M.-I. Pujol[4], M. Ballarotta[4], I. Durand[1], and C. Provost[1]

[1]Laboratoire LOCEAN-IPSL, Sorbonne Université (UPMC, Univ. Paris 6)-CNRS-IRD-MNHN, Paris, France, [2]Korea Polar Research Institute, Incheon, South Korea, [3]Korea Institute of Ocean Science and Technology, Busan, South Korea, [4]Collect Localisation Satellites, Ramonville Saint-Agne, France

Key Points:
- The Antarctic Circumpolar Current is only 170 km wide in the Udintsev Fracture Zone, forming the narrowest circumpolar choke point
- First observations of high-quality hydrography in the Udintsev Fracture Zone show no Antarctic bottom water colder than 0.2 °C
- The Udintsev Fracture Zone is a suitable site for a long-term monitoring of the Antarctic Circumpolar Current

Correspondence to:
Y.-H. Park,
young-hyang.park@mnhn.fr

Citation:
Park, Y.-H., Park, T., Kim, T.-W., Lee, S.-H., Hong, C.-S., Lee, J.-H., et al. (2019). Observations of the Antarctic Circumpolar Current over the Udintsev Fracture Zone, the narrowest choke point in the Southern Ocean. *Journal of Geophysical Research: Oceans*, *124*, 4511–4528. https://doi.org/10.1029/2019JC015024

Received 1 FEB 2019
Accepted 13 MAY 2019
Accepted article online 22 MAY 2019
Published online 4 JUL 2019

Abstract An up-to-date map of the Antarctic Circumpolar Current (ACC) fronts is constructed from the latest version of mean dynamic topography (MDT) from satellite altimetry and reveals the narrowest ACC width in the Udintsev Fracture Zone (UFZ), with the strongest concentration of the three major ACC fronts within a limited distance as short as 170 km, about 40% narrower than that at Drake Passage. At 144°W, at the entrance of the UFZ, which lies between the Pacific-Antarctic Ridge (PAR) and its eastwardly offset segment (offset PAR segment), there is a triple confluence of the Subantarctic Front, Polar Front, and Southern ACC Front . Downstream of this longitude, the Subantarctic Front progressively meanders northward over the relatively shallow offset PAR segment before channeling through the Eltanin Fracture Zone, thus diverging from the Polar Front which proceeds through the UFZ. In situ observations from two recent cruises at 144°W confirm the satellite altimetry-derived frontal circulation in the UFZ region and yield a baroclinic transport relative to the bottom of 113×10^6 m^3/s, comparable to that through Drake Passage. The hydrographic sections show no Antarctic bottom water colder than 0.2 °C. Characteristics of major water masses are described, and the implications for their potential downstream modifications at Drake Passage are discussed in terms of the meridional overturning circulation across the ACC. Mesoscale eddy activity with periods shorter than 90 days is predominantly concentrated in the immediate downstream area of the offset PAR segment, suggesting a substantial poleward eddy heat flux there.

1. Introduction

The Antarctic Circumpolar Current (ACC) forms a continuous near-zonal band of eastward flow. The width of the band, however, is not uniform, rather it is marked by several "choke points" due to strong steering of flow by the prominent ridge systems around Antarctica, such as the complex ridge system in Drake Passage, the Southwest Indian Ridge, the Kerguelen Plateau, the Macquarie Ridge south of Tasmania, the Udintsev Fracture Zone (UFZ)/Eltanin Fracture Zone (EFZ) in the central South Pacific sector, and so forth. The best known choke point is Drake Passage where the ACC is constricted to a narrow geographical region between the southern tip of South America and the northern tip of the Antarctic Peninsula. These choke points are characterized by narrowly concentrated frontal zones of deep-reaching currents and associated with enhanced eddy activity especially downstream of prominent topographic features. The eddy-mean flow interaction in the latter areas has an important climate implication for the poleward transport of heat and vorticity (Abernathey & Cessi, 2014; Thompson & Sallée, 2012; Williams et al., 2007), thus constituting a key element of the meridional overturning circulation of the Southern Ocean.

Previous studies of the ACC fronts (Belkin & Gordon, 1996; Orsi et al., 1995; Sokolov & Rintoul, 2009, among others) systematically show a tight channeling of the ACC through the two parallel fracture zones about 4–5° in latitude apart, the UFZ and EFZ in the central South Pacific sector. This suggests that topographic steering is the major dynamic factor controlling the magnitude and direction of the ACC in these fracture zones. These fracture zones correspond to the NW-SE elongated linear bathymetric features resulting from the tectonic action of offset mid-ocean ridge axis segments (Figure 1). As a consequence, the Pacific-Antarctic Ridge (PAR) is disconnected both from the East Pacific Rise (EPR) and an unnamed segment of offset ridge axis in between the two, which we call tentatively as "offset PAR segment." The major bathymetric feature of the UFZ is found between the northern escarpment of the PAR and the southern escarpment of the offset

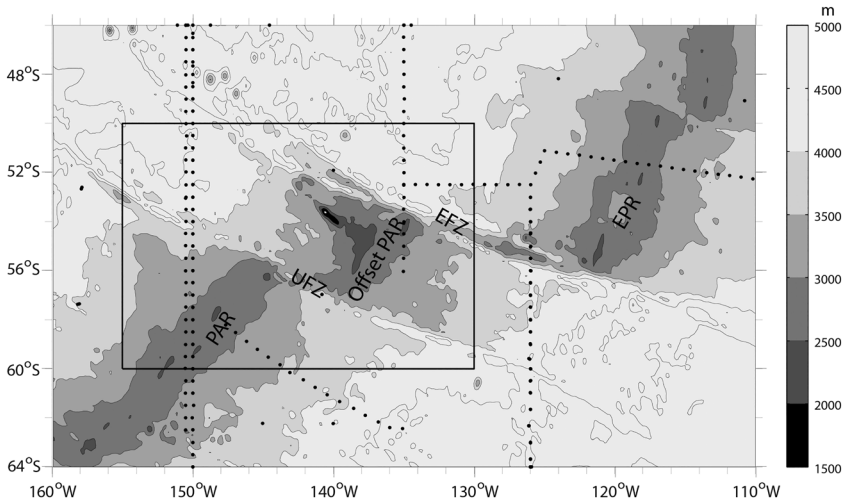

Figure 1. Major bathymetric features and fracture zones in the central South Pacific sector of the Southern Ocean: Pacific-Antarctic Ridge (PAR), offset PAR segment, East Pacific Rise (EPR), Udintsev Fracture Zone (UFZ), and Eltanin Fracture Zone (EFZ). The study area (solid rectangle) and historical, high-quality hydrographic sections (dotted lines, http://www.nodc.noaa.gov/OCL/) are superposed.

PAR segment, whereas that of the EFZ is between the northern escarpment of the offset PAR segment and the southern escarpment of the EPR. Several hydrographic sections have been made in the upstream and downstream areas of the UFZ especially during the 1990s World Ocean Circulation Experiment (WOCE) period, such as WOCE P16 at 150°W and WOCE P17 at 135°W (Figure 1; Gille, 1999). However, no high-quality top-to-bottom hydrography has ever been performed in the UFZ itself at 144°W.

As part of the ongoing PHANTOM (Poleward Heat Transport across the ACC) program of LOCEAN/Sorbonne University, we have recently occupied two full-depth Conductivity-Temperature-Depth/Oxygen (CTD/O_2) sections in the UFZ region during a current-meter mooring deploying cruise in February 2016 and a mooring recovery cruise in December 2017 onboard the Korean icebreaker Araon, in collaboration with physical teams of Korea Polar Research Institute and Korea Institute of Ocean Science and Technology. Here we document the local frontal structure of the ACC and associated large-scale circulation based on the CTD/O_2 observations combined with historical hydrographic data. In this study satellite altimetry is essential for inferring the climatological locations of the ACC fronts and for accessing the spatiotemporal variability of the surface circulation as the currents negotiate the fractured ridge system of the region. Analysis of the current meter data is in progress and is not reported here. Our major objective herein is to prepare a background picture of the frontal structure and local circulation pattern of the ACC in this potentially important but poorly documented choke point and lay the foundation of future analysis of the current meter data.

The paper is organized as follows. The data are presented in section 2. In section 3, we first review the hydrography-based traditional definition of the major ACC fronts. This is followed by the determination of climatological mean locations of the ACC fronts from altimetry, which are then validated in the UFZ region against Argo hydrography-derived fronts. Section 4 presents recent ACC observations in the UFZ region. Frontal structure and characteristics of water masses in the hydrographic sections are described, and bottom-referenced baroclinic currents and transport are presented. Section 5 deals with the spatiotemporal variability of the regional circulation by tracking synthetic particles and mapping eddy and mean kinetic energy (MKE) from altimetry. Section 6 summarizes and discusses the implications of the results.

2. Data

2.1. Hydrographic Data

In February 2016, we occupied a full-depth CTD/O_2 section across the UFZ along the Jason altimeter ground track 219 onboard the Korean icebreaker Araon (Figure 2). This section, called hereafter as the A section, starts at 58°S, 147.5°W and ends at 53°S, 141°W and comprises a total of 12 CTD/O_2 stations. The

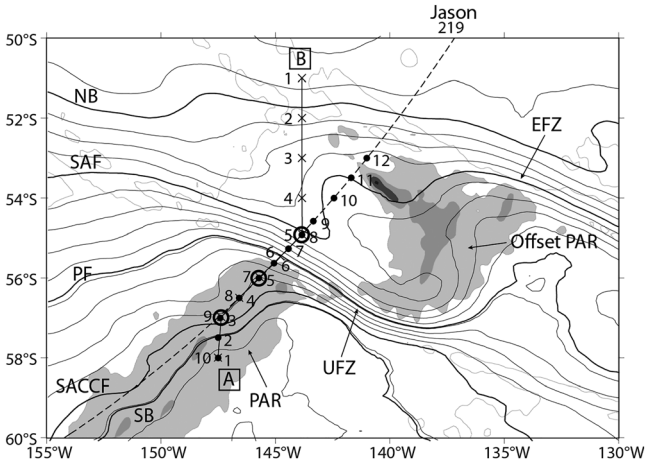

Figure 2. Map showing the two Conductivity-Temperature-Depth/Oxygen sections occupied in February 2016 (A section with dots) and December 2017 (B section with crosses), overlaid on the zoomed streamlines and Antarctic Circumpolar Current fronts of Figure 3. Three lines of current meter moorings are indicated by circles. The Jason altimeter ground track 219 is indicated with a dashed line. Other comments are same as in Figures 1 and 3. Depths shallower than 3,000, 2,500, and 2,000 m are increasingly darkly shaded.

southern part of the A section runs over the SW-NE-oriented PAR which is disconnected by the UFZ from the offset PAR segment. The northern part of the A section passes through the immediate upstream area of the latter ridge segment. Due to the limited cruise time, the A section could cover all but the northern flank of the ACC. During the mooring recovery cruise in December 2017, a new CTD/O_2 section, referred to as the B section, was made from north to south along a meridional track at 144°W in its northern part north of 55°S and repeated the same track as the A section in its southern part. This time, the B section covered the full breadth of the ACC, occupying a total of 10 CTD/O_2 stations between 51°S and 58°S. The CTD sensors were calibrated before and after the cruise, and the postcruise validated data for pressure, potential temperature, salinity, and dissolved oxygen (bottle data) are thought to be accurate within ±3 dbar, ±0.003°C, ±0.005 psu, and ±0.005 ml/L, respectively.

We do not present the current meter data which will be reported elsewhere, except for some preliminary information about the bottom currents at two mooring sites. In addition to the just described in situ hydrographic data, we also use hydrographic data gathered in the UFZ region via Argo floats (http://www.coriolis.eu.org/Data-Products/Data-Delivery/Data-selection) in order to validate the climatological ACC fronts from altimetry. Note that all bathymetry described in this paper is based on the ETOPO2 data (https://www.ngdc.noaa.gov/mgg/global/etopo2.html).

2.2. Satellite Altimetry

Satellite altimetry forms a backbone of the present study for putting the local ACC frontal observations within the entire circumpolar context as well as for documenting the spatial and temporal variability of the fronts. It serves as a useful reference for foreseeing the frontal positions during the preparation of the cruise as well as for the postcruise validation comparing with in situ observations. Climatological positions of major ACC fronts are derived from the 1/8°-resolution MDT of Centre National d'Etudes Spatiales-Collect Localisation Satellites 2018 (CNES-CLS18) for the 1993–2012 reference period (Rio et al., the new CNES-CLS18 MDT solution, 2019, personal communication). This new solution was calculated using the CNES-CLS15 altimetric Mean Sea Surface (Pujol et al., 2018), the latest Gravity field and steady-state Ocean Circulation Explorer (GOCE) geoid model, GOCO05c (Fecher et al., 2017), as well as an extended data set of in situ observations (Surface Velocity Program (SVP) -type drifting buoy velocities and Argo floats covering the period 1993–2016). Compared to the previous versions such as the CNES-CLS09 MDT (Rio et al., 2011) or CNES-CLS13 MDT (Rio et al., 2014), significant improvement is achieved when comparisons are made with independent observations of surface currents, in particular in coastal areas and in strong currents (Rio et al., the new CNES-CLS18 MDT solution, 2019, personal communication). Eddy activity of the surface flow is inferred from the global ocean 1/4°-resolution daily anomalous velocity data for 1993–2018, corresponding to the DT2018 altimeter standards (Taburet et al., 2019) distributed by European Copernicus Marine Environment Monitoring Service (http://marine.copernicus.eu/services-portfolio/access-to-products/). We also use the regionally optimized velocity anomaly product at high temporal (daily) and spatial (1/8°) resolution for 6 months from November 2015, which has been specially prepared for our study area by CLS with support from CNES. These data were processed using the same upstream products as the DT2018 global version and benefit from new dynamical mapping techniques able to propagate the mesoscale structures more accurately (Ubelmann et al., 2015). These high-resolution data are used here for documenting the frontal circulation interacting with local bathymetric features by tracking time-varying particle trajectories in the study area.

3. Climatological Mean Locations of the ACC Fronts

3.1. Definitions: A Review

Before the satellite altimetry era, prior to the 1990s, oceanic fronts in the Southern Ocean had been nearly entirely defined from hydrographic observations. An eastward flow in the Southern Ocean exhibits

poleward sloping isopycnals due to the geostrophic balance of the mass field; hence, the ACC fronts can be identified as the locations where jet-like currents are associated with a steep rise of isopycnals toward the south throughout the water column. A clear-cut example of this across Drake Passage may be seen in Nowlin et al. (1977) who showed three to four bands of bottom-reaching strong currents over steeply sloping isopycnals with surface velocities greater than 0.2 m/s, distinguishable from sluggish zones of velocities weaker than 0.1 m/s over moderately sloping isopycnals.

As the strongest currents are mostly associated with the upper-layer baroclinic structure, the front detection from hydrography often uses specific criteria of property values at some selected subsurface levels. The most frequently cited level is the 200-m level especially for the Polar Front (PF), which is traditionally defined as the northernmost extent of subsurface temperature minimum layer (T_{min}) or Winter Water of 2 °C (Botnikov, 1963). This PF definition has been most widely and probably unanimously accepted in the literature (e.g.,Belkin & Gordon, 1996 ; Orsi et al., 1995 ; Park et al., 1993 ; Whitworth & Nowlin, 1987). The Subantarctic Front (SAF) often coincides with the beginning of northward descent below 400 m of the salinity minimum layer (S_{min}) or Antarctic Intermediate Water (Whitworth & Nowlin, 1987), which can be identified near the 4–5 °C isotherms at 400 m (Orsi et al., 1995) or with the 200-m axial isotherms between 4 and 6 °C depending on circumpolar locations (Belkin & Gordon, 1996). The latter authors emphasized the circumpolar robustness of structural criteria applied to vertical thermohaline structure/stratification to track all major fronts of the Southern Ocean from 0°E to 150°E. According to Belkin and Gordon (1996), three structural elements are observed north of the SAF, namely, (1) thick (>400 m) layer of nearly uniform water called Subantarctic Mode Water, (2) subsurface salinity maximum (S_{max}), and (3) intermediate S_{min}. In contrast to the single jet of the conventional SAF, Sokolov and Rintoul (2002) suggested three branches of the SAF based on temperature criteria at the 300- to 400-m depth range, namely, 6–8 °C for the northern SAF (SAF-N); 5–6 °C for the middle SAF; 3–5 °C for the southern SAF. The conventional SAF matches most closely with the middle SAF. Finally, Orsi et al. (1995) defined the Southern ACC Front (SACCF) at the Greenwich Meridian near the 0 °C T_{min} at a depth of <150 m or at the subsurface temperature maximum (T_{max}) of 1.8 °C. However, these dual criteria of the SACCF are not always compatible with each other in the other sectors of the Southern Ocean. This incompatibility is particularly pronounced in the Indian sector especially in the Enderby Basin where the 1.8 °C T_{max} is located systematically farther south by several hundred kilometers as compared to the 0 °C T_{min} (Roquet et al., 2009). Therefore, the 1.8 °C T_{max} criterion is not taken into consideration in this paper. Orsi et al. (1995) attributed the 1.6 °C T_{max} criterion to the front associated with the southern boundary (SB) of the ACC, which in the Fawn Trough is located near the subsurface T_{min} between 0 and −1 °C (Park et al., 2009).

In order to check whether the above-mentioned structural and subsurface temperature criteria are applicable to our study area, Figure 6 presents the thermohaline structure and geostrophic velocity field for the first 1,500 m across the repeat WOCE P16S section at 150°W occupied in April 2014 (https://cchdo.ucsd.edu/cruise/320620140320). There appear three well-distinct jets with a peak surface velocity exceeding >0.2 m/s at 51°45′S, 54°S, and 56°45′S. Referring to the upper-mentioned structural criteria as well as subsurface temperature criteria at fixed depths for the SAF, the northernmost jet corresponds to the SAF-N, the strongest (>0.4 m/s) middle jet to the conventional SAF, and the southernmost jet to the PF. In the 200- to 500-m depth range, the SAF-N coincides with a steep horizontal gradient across the 7–9 °C isotherms, with a sharp northward rise in salinity >34.5 and a much weakened vertical stratification to the north of the front, indicative of the Subantarctic Mode Water thermostad (Belkin & Gordon, 1996). The SAF coincides with a steep gradient between isotherms 5 and 6 °C in the 200- to 400-m depth range and marks the beginning of the deepening of S_{min} below 400 m, a well-known structural criterion of the conventional SAF (Whitworth & Nowlin, 1987). This is also consistent with the structural criteria of Belkin and Gordon (1996) for the SAF. There is no ambiguity for identifying the PF which is located between subsurface T_{min} isotherms 1 and 2 °C that are very close to each other at 150 m. No significant jet is attributable to both the SACCF and SB.

3.2. Climatological Circumpolar Fronts From Satellite Altimetry

The CNES-CLS18 MDT represents the mean surface geostrophic streamlines, and surface geostrophic velocities are calculated by simple finite difference (Figure 3). The three major fronts (SAF, PF, and SACCF) of the ACC are identified as well as its northern boundary (NB) and SB, which we consider as part of the ACC fronts as property characteristics change abruptly across these boundaries, as will be seen in section 4.

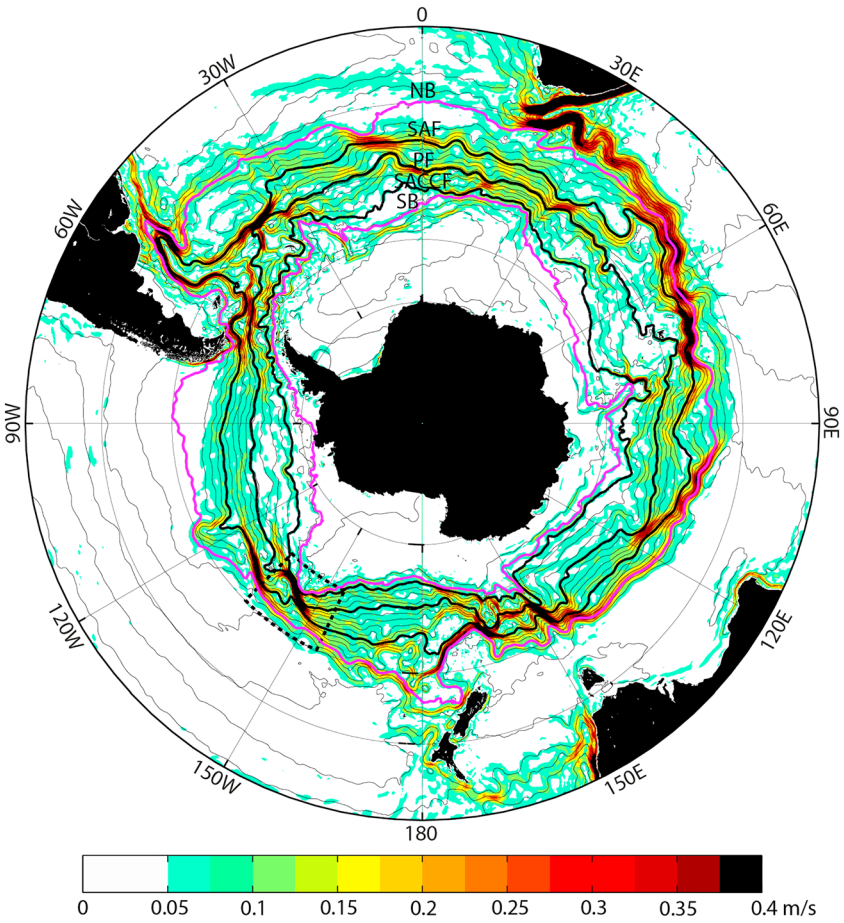

Figure 3. Mean Dynamic Topography (light black lines every 0.1 m) of the Southern Ocean from the Centre National d'Etudes Spatiales-Collect Localisation Satellites 2018 Mean Dynamic Topography data set. Thick black lines stand for three major Antarctic Circumpolar Current fronts, from the north: SAF ≡ −0.10 m, PF ≡ −0.58 m, and SACCF ≡ −1.00 m. The NB and SB of the Antarctic Circumpolar Current (NB ≡ 0.30 m, SB ≡ −1.11 m) are indicated by thick magenta lines. The intensity of surface geostrophic currents is shown with color (m/s). The dotted black polygon designates the study area. NB = northern boundary; SAF = Subantarctic Front; PF = Polar Front; SACCF = Southern Antarctic Circumpolar Current Front; SB = southern boundary.

Figure 3 is the latest version of similar maps based on the previous version CNES-CLS09 MDT (Kim & Orsi, 2014; Park et al., 2009), which are globally alike, although some notable differences exist at places. Note only that the SB from the CNES-CLS18 MDT presented here approaches most closely Antarctica in the Bellingshausen and Amundsen Seas region, even touching the Antarctic coast at 100°W, which has been particularly ill defined from the CNES-CLS09 MDT (Kim & Orsi, 2014) or CNES-CLS13 MDT (not shown) due to frequently disconnected, irregular-isolated MDT segments in this high latitude area. The closest approach of the SB to the Antarctic coast at 100°W should have great climatic implications for warm deep water flooding the continental shelf and sustaining the warm shelf bottom water regime (0–1.5 °C) unique in the Bellingshausen and Amundsen Seas (Thompson et al., 2018), thus acting to modulate the melting of the West Antarctic Ice Sheet.

The streamlines corresponding to the above five circumpolar fronts are determined as follows. First, the ACC northern and southern boundaries are unambiguously defined as those circumpolar streamlines passing through the northernmost and southernmost latitudes of Drake Passage, coinciding with the MDT contour of 0.30 m for the NB and −1.11 m for the SB. There is no great alternative for defining these boundaries because their streamlines are constrained by continental slopes at Drake Passage. Outside of Drake Passage, the separation of the ACC from adjacent gyres is not an easy task. Therefore, the definition of the equatorward and poleward limits of the ACC from altimetry is very useful especially for making difference between

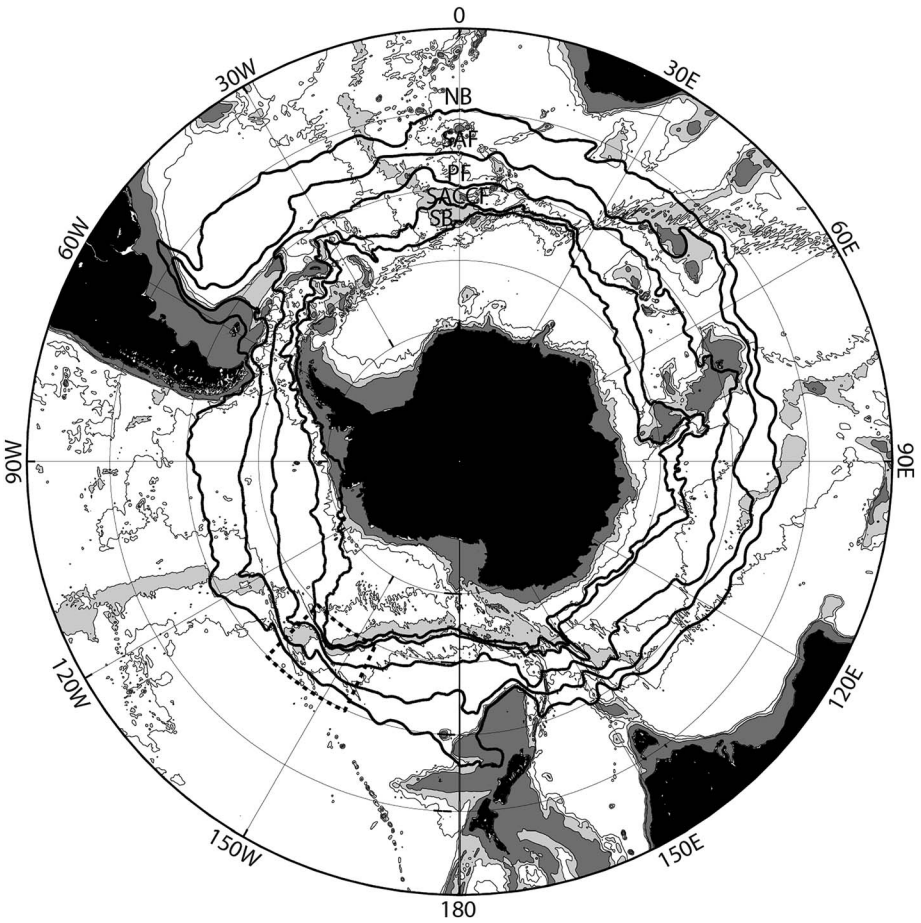

Figure 4. The five Antarctic Circumpolar Current fronts (NB, SAF, PF, SACCF, and SB) from Figure 3 are superposed on prominent topographic features. Isobaths 2,000, 3,000, and 4,000 m are indicated, and depths shallower than 2,000 (3,000) m are heavily (lightly) shaded.

the ACC water masses from those of adjacent subtropical and subpolar gyres as well as for separating the currents and transport associated with the ACC from those outside of the ACC band. While the SB has previously been defined from hydrography (Orsi et al., 1995) or altimetry (Kim & Orsi, 2014; Park et al., 2009; Sokolov & Rintoul, 2009), the definition of the NB from altimetry seems new. Note however that our NB runs close to the northern branch of the SAF (SAF-N) in Sokolov and Rintoul (2009) and Barré et al. (2011). Indeed, it is shown in the following subsection that the newly defined NB from altimetry matches well with the SAF-N identified from hydrography in the study area. Therefore, the altimetry-derived NB and the hydrography-derived SAF-N are used interchangeably in this study.

Once the northern and southern boundaries of the ACC (NB and SB) are determined, the other three fronts (SAF, PF, and SACCF) should be found in between them. These fronts are systematically associated with concentrated strong jets (>0.2–0.3 m/s) at the major choke points formed in the vicinity of deep passages or prominent topographic features of submarine ridge systems in the regions such as (Figure 4) UFZ, Drake Passage, Southwest Indian Ridge at 30°E, Kerguelen Plateau, and south of Tasmania/Macquarie Ridge. At these choke points, each front is associated with a particular MDT contour most common to all choke points: SAF = −0.10 m; PF = −0.58 m; SACCF = −1.00 m, which are very close to the values corresponding to the central branches of those fronts in Barré et al. (2011). The choice of these streamlines is not arbitrary but is constrained by well-defined frontal positions from both altimetry and hydrography. The best streamlines for the SAF and PF should correspond to those passing directly through the EFZ and UFZ, respectively, which are clearest in Figure 4 by the presence of two well-separated strong jets channeled through these fracture zones. The circumpolar locations of these two fronts should be also consistent with

representative hydrographic observations in Drake Passage (Nowlin et al., 1977; Provost et al., 2011, among others), in the Scotia Sea (Meredith et al., 2003), across the Southwest Indian Ridge at 30°E (Park et al., 2001), around the Crozet Plateau (Pollard et al., 2007), around the Kerguelen Plateau (Park et al., 2014), and south of Tasmania (Sokolov & Rintoul, 2002). For example, the optimal circumpolar streamline of the PF should round the Kerguelen Islands (49°S, 70°E) from the south (not north), hugging the southern and eastern escarpments (500- to 1,000-m isobaths) around the islands, in agreement with the climatological positions of the northern limit of Winter Water <2 °C of the region, as verified by an extended survey of the Kerguelen PF frontal zone during the 2011 KEOPS2 cruise (Park et al., 2014). Also, the optimal SAF should show a well-defined S-shape meander around the Del Cano Rise (45°S, 46°E), as unambiguously identified by Pollard et al. (2007) from hydrographic sections, Argo floats, surface drifters, and satellite altimetry. Similarly, the reference hydrographic studies best validating the SACCF have been carried out across the Fawn Trough of the Kerguelen Plateau by Park et al. (2009) and Roquet et al. (2009) and in the Scotia Sea by Meredith et al. (2003).

There appears an outstanding choke point comparable to or even narrower than Drake Passage in the central South Pacific sector (dotted polygon in Figures 3 and 4) far from the continental boundaries. There, we observe the concentration of the three major ACC fronts within a narrow latitudinal stretch of 1.5° at the entrance of the UFZ at 144°W. The SACCF flows northeastward along the northern flank of the PAR from the dateline until 144°W where it converges with the combined PF and SAF before crossing the ridge system over the fracture zones. Downstream of this longitude, the combined SACCF and PF pass southeastward through the UFZ, while the SAF progressively meanders northeastward to pass through the EFZ. The triple convergence of the three major ACC fronts at 144°W appears as the narrowest choke point of the entire Southern Ocean, which will be further quantified below.

Outside of the above choke point regions, the ACC surface velocities drop by a factor of 2 to 3 especially in the southern part of the ACC south of the PF. This is consistent with a downstream divergence of streamlines, spreading the weakened flow over extended latitudinal breadth until their reconvergence on approaching downstream choke points. In these weak flow regimes, the streamlines associated with the major ACC fronts defined in the choke point regions do not always coincide with current cores that are rather sporadic and often skip from one streamline to another, making the tracking of a continuous circumpolar front unlikely. Best example of this can be seen south of the PF in the Enderby Basin of the Indian sector, the Australian-Antarctic Basin, and the eastern South Pacific sector downstream of the UFZ. Moreover, currents there are very weak with their intensity mostly less than 0.1 m/s, a value corresponding to a sluggish flow regime in between the major ACC fronts in Drake Passage. Consequently, a number of interrupted segments of weak current are interweaving with adjacent streamlines, disabling continuous circumpolar front detection, as previously remarked by Hughes and Ash (2001). In contrast, satellite altimetry appears most useful for defining the climatological mean ACC fronts in the vicinity of the major choke points.

A Mercator projection of the ACC fronts (Figure 5a) facilitates the appreciation of the latitudinal distance of each front from the PF as a function of longitude (Figure 5b). Among all choke points, the UFZ region at 144°W appears as the prime choke point of the whole circumpolar longitudes, with the narrowest ACC breadth of about 500 km between the NB and SB and the strongest concentration of the three major ACC fronts (SAF, PF, and SACCF) within a distance as short as ~170 km. This UFZ choke point is even narrower than that in Drake Passage (SAF-SACCF distance of ~270 km at 58°W) by 40%, although the latter region has previously been considered as the narrowest constriction of the ACC.

Finally, it is to be noted that the SB is generally associated with the weakest flow within the ACC while the NB in the Indian sector and south of Australia with the strongest flow especially in the subtropical frontal zone between the Crozet and Kerguelen Plateaus (see Figure 3). This is likely due to a tight confluence of the ACC with the powerful Agulhas Return Current flowing along the southern limb of the South Indian subtropical gyre, as clearly demonstrated in the Crozet Basin from the SUZIL cruise (Park et al., 1993). Outside of these subtropical confluence regions, the strongest ACC flow tends to be concentrated in the SAF and PF or in between them. It is also remarkable that secondary jet-like features (with peak velocities of $O(0.2$ m/s); yellow to orange shading in Figure 3) often appear in between the SAF and PF especially in regions immediately downstream of the major choke points. As MDT streamlines are geostrophic streamlines, thus cannot cross each other by definition, and considering high eddy activity in frontal regions, the

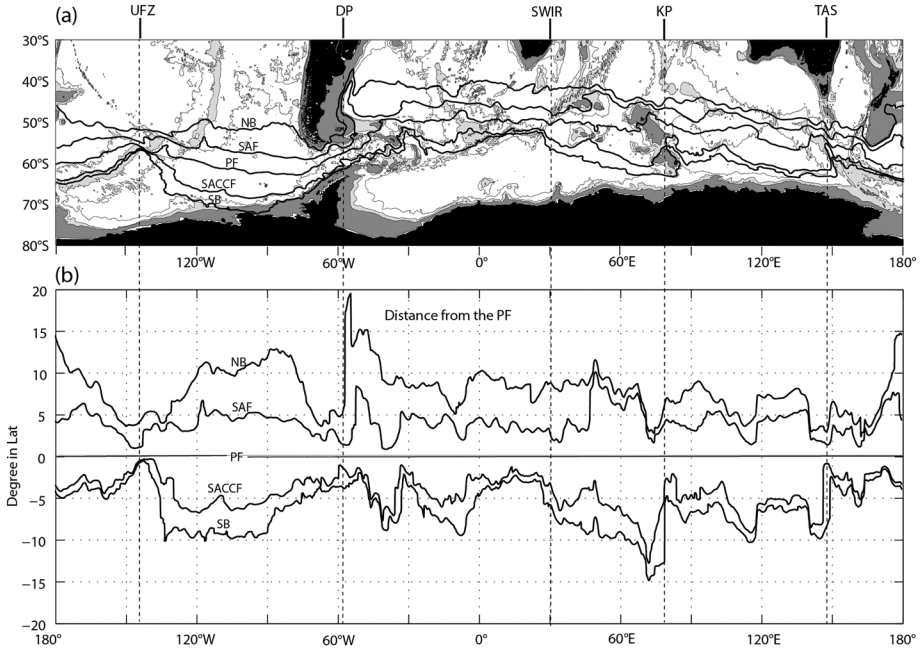

Figure 5. (a) The five Antarctic Circumpolar Current fronts with topography of Figure 4 but on a Mercator projection. Big five choke points are indicated, from the west: UFZ = Udintsev Fracture Zone; DP = Drake Passage; SWIR = Southwest Indian Ridge; KP = Kerguelen Plateau; TAS = Tasmania. (b) Meridional distance (*y* axis, degree in latitude) of each front from the Polar Front (PF) as a function of longitude (*x* axis).

observed secondary jet-like features in between adjacent major ACC fronts are believed to have been generated by eddy-mean flow interaction through the convergence of meridional eddy momentum flux (e.g., Hoskins et al., 1983). However, a detailed assessment for the latter subject deserves further investigation.

3.3. Climatological ACC Fronts in the UFZ Region Based on Argo Float Hydrography

In order to identify the climatological locations of the major ACC fronts from hydrography, a map of subsurface T_{min} in the 100- to 250-m depth range is prepared using all available Argo float data (23,073 profiles) collected during the 2001–2017 period in the study area (Figure 7). Colored dots represent subsurface T_{min} from floats, and isotherms every 1° between −1 and 8 °C are shown by black lines, in comparison with altimetry-derived fronts (thick red lines). In this figure T_{min} isotherms found to the north of the PF are indistinguishable from those isotherms at a constant depth of 250 m as temperature to the north of the PF decreases monotonously with increasing depth. Isotherms matching most closely with the altimetry-derived fronts are emphasized with thick black lines (Figure 7). We observe that the altimetry-derived NB matches most closely with the 7 °C isotherm, although to the west of 147°W, it is located in slightly warmer water in between the 7 and 8 °C isotherms corresponding to the SAF-N, consistent with Figure 6. This close match between the SAF-N and the NB may further justify why the terms NB (from altimetry) and SAF-N (from hydrography) are used interchangeably in this paper. Similarly, the 5 °C isotherm in Figure 7, which is consistent with the subsurface isotherms associated with the SAF in Figure 6, coincides with the altimetry-derived SAF. Recall that the geographical locations of the altimetry-derived SAF have been determined so as to match most closely with those of the well-established conventional SAF at different choke points. The 2 and 0 °C T_{min} isotherms corresponding to the PF and SACCF, respectively, agree in location with their altimetric counterparts especially to the east of 150°W. Finally, the altimetry-derived SB is not well associated with any particular T_{min} isotherm. Moreover, the −1 °C isotherm is particularly ill defined in the south central part of the area due to very limited float data there.

Aside from a few local exceptions, these Argo hydrography-derived ACC fronts (thick black lines) mostly superpose within ±0.5° in latitude on altimetry-derived fronts (thick red lines), giving us great confidence

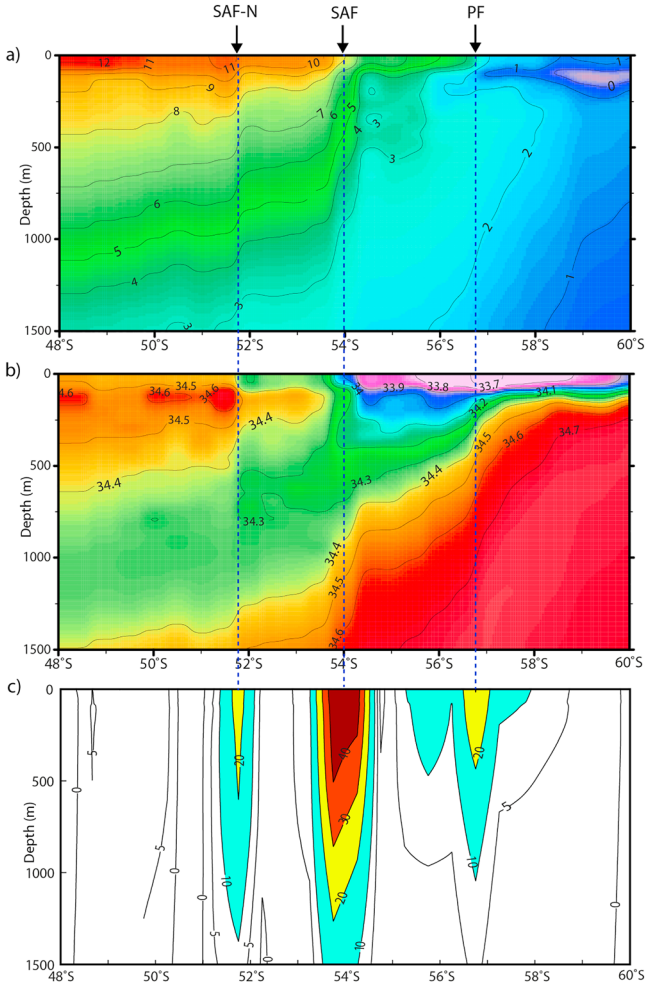

Figure 6. (a) Potential temperature (°C), (b) salinity (psu), and (c) across-section geostrophic velocity (cm/s) relative to the bottom along the finely resolved (1/2°) repeat World Ocean Circulation Experiment section at 150°W. The dashed vertical lines correspond to the cores of three well-distinct jets. Velocities every 10 cm/s are color shaded. SAF-N = northern SAF; SAF = Subantarctic Front; PF = Polar Front.

for safely using the latter fronts. Artana et al. (2016) also pointed out a good match in the Malvinas Current region between altimetry-derived fronts based on the Barré et al. (2011) criteria defined in the Drake Passage region, which are very close to ours, and Argo hydrography-derived fronts based on potential density criteria at 400 m. Note however that the Argo-derived fronts in Figure 7 present a number of mesoscale eddy-like fluctuations overlaid on more smoothly undulating isotherms, with the latter feature well corresponding to a larger-scale pattern of altimetry-derived fronts. We suspect that the smaller-scale spatial undulations seen in Argo-derived fronts might be partly associated with temporal aliasing due to irregular undersampling in space and time of Argo data compared to altimetry.

The most remarkable feature in the climatological locations of the ACC fronts in the UFZ region (Figure 7) is a tight confluence at the UFZ entrance at 144°W of relatively warm subsurface water (~5 °C) associated with the SAF and the 0 °C Winter Water associated with the SACCF within a limited meridional distance as short as 1.5° in latitude, with the PF being sandwiched between them. This confluence results from a gradual southeastward deflection of the SAF and a northeastward flow of the combined SACCF/SB along the PAR, yielding shrinkage of the ACC width at 144°W by a factor of 4 compared to an upstream longitude at 155°W (Figure 2). Note that the SB is located precisely on the PAR axis to the west of 147°W. Downstream of the 144°W confluence, the SAF retroflects northward and then eastward, forming an S-shape meander and crosses the offset PAR segment to the north before passing through the EFZ. This S-shape meander is likely the consequence of topographic control of Hollister Ridge (Vlastélic & Dosso, 2005), a NW-SE oriented shallow ridge <2,000 m centered at 53°45′S, 140°30′W in the northwestern corner of the offset PAR segment (Figure 2). The PF channeled in the UFZ consistently flows southeastward, although at the exit of the UFZ the northern branch of the PF sharply turns northward along the eastern flank of the offset PAR segment to approach the SAF. Nevertheless, there appears a complete separation of the SAF through the EFZ along the northern escarpment from the PF through the UFZ along the southern escarpment of the offset PAR segment (Figure 2).

4. In Situ Observations of the ACC Fronts in the UFZ Region

4.1. Frontal Structure and Surface/Subsurface Water Masses

Property sections along the A section (Figure 8a) are shown compared with those along the B section (Figure 8b), as well as corresponding potential temperature-salinity (θ-S) and potential temperature-oxygen (θ-O_2) diagrams (Figure 9). Consistent with climatology (Figures 2 and 7), the A section cuts the SAF three times at latitudes of 54°55′S, 54°20′S, and 53°10′S, which are found all within ±0.25° in latitude from the climatological SAF locations derived from both altimetry and hydrography. The B section, which runs in its northern part along 144°W and a common part with the section A south of 55°S, cuts the SAF only once at about 55°S, also consistent with climatology. At these SAF locations, the upper 200 m is characterized with low-salinity (<34.1–34.2), relatively warm (~5°C), and moderate oxygen content (>6 ml/L). Note that the sharp horizontal thermal gradient at 200 m between the 3 and 5 °C isotherms on the B section (Figure 8b) is not inconsistent with the reported range (4–6 °C) of axial temperature at 200 m for the SAF (Belkin & Gordon, 1996). Furthermore, both altimetry and hydrography (Figures 2 and 7) indicate unambiguously that the SAF crossing the 144°W longitude is the continuation of the upstream SAF at 150°W (Figure 6), which corresponds to the conventional SAF, as already mentioned.

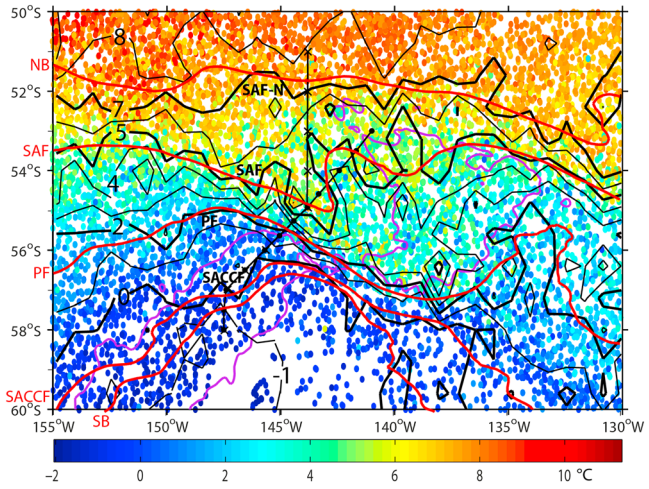

Figure 7. Minimum temperature (T_{min}) at the subsurface (100–250 m) layer from best available Argo float data (23,073 profiles over 2001–2017) in the study area. Color dots represent the Argo float profile location. The T_{min} isotherms best matching with altimetry-derived fronts (thick red lines) are emphasized with thick black lines. The 3,000-m isobath (violet lines) and the two Conductivity-Temperature-Depth/Oxygen sections discussed in the text are also indicated. SAF-N = northern SAF; SAF = Subantarctic Front; PF = Polar Front; NB = northern boundary; SACCF = Southern Antarctic Circumpolar Current Front; SB = southern boundary.

The PF, which is best characterized with the 2 °C T_{min} at <200 m and the lowest surface salinity (<33.9–34.0) of the section, is located at 55°35′S along both sections, in good agreement with climatology. Along the A section, we also observe an isolated patch of T_{min} <2 °C with relatively low salinity and high dissolved oxygen centered at 53°30′S (Figure 8a), which is absent along the B section (Figure 8b). This isolated T_{min} north of the PF along the A section should be related to the quasi-permanent S-shape meandering of SAF, although climatology (Figure 7) shows no T_{min} <2 °C within the SAF meander centers. We think therefore that this isolated T_{min} at 53°30′S might have been caused by a transient cold eddy detached from a highly perturbed unstable PF sometime prior to the occupation of the A section. In effect, animation of altimetry-derived instantaneous surface velocity fields (not shown) gives clear evidence of a cyclonic eddy pinched-off, a month prior to the cruise, from a northward elongated meander of the combined SAF/PF. No such mesoscale eddy activity is evident in the B section.

The SACCF is distinct from the PF especially in the θ-S and θ-O_2 diagrams of the finely resolved (mostly 0.5° in latitude) A section (Figures 9a and 9c) where the well-oxygenated (>7.2 ml/L) cold (<0 °C) T_{min} water associated with the SACCF near station 4 is clearly separated from the less oxygenated (>6.8 ml/L) and much warmer (<2 °C) T_{min} water associated with the PF near station 6. The corresponding T_{max} is also distinct: 2.2 °C at the SACCF compared to 2.5 °C at the PF. This hydrography-derived SACCF location on the A section (Figure 8a) is within 0.25° in latitude from the altimetry-derived climatological location (Figure 2). On the other hand, the exact location of the SACCF on the B section is difficult to ascertain because of a large station interval of 1° in latitude between the two southernmost stations 9 and 10, although we have tentatively placed the front midway of station 9 and the SB discussed below.

Finally, the SAF-N and SB can also be identified by abrupt meridional changes in the surface layer properties, which are most apparent on the B section in the vertical property sections (Figure 8b) or in the θ-S and θ-O_2 diagrams (Figures 9b and 9d). Accordingly, we assign the SAF-N on the B section (144°W) at 51°30′S, halfway between two northernmost stations, but with a large uncertainty (0.5° in latitude) ascribed as a half of the station interval of these stations. This hydrography-derived SAF-N agrees, within the above uncertainty, with the altimetry-derived NB at 51°45′S (Figure 2). Surface water characteristics north of the SAF-N are clearly of subtropical origin with the warmest (>10 °C) and saltiest (>34.45) water of the section, whereas those south of the SAF-N are colder than 8 °C and fresher than 34.2. Similarly, the SB at 147.5°W is assigned at 57°45′S in between two southernmost stations for the finely resolved A section and at 57°30′S for the loosely resolved B section, although the latter latitude fortuitously coincides with the altimetry-derived climatological SB location (Figure 2). T_{min} Winter Water at the southernmost station located south of the PAR axis shows distinct subpolar characteristics ($\theta < -1$ °C, $S \sim 34.3$) and is associated with the coldest T_{max} (<1.5 °C) in either section.

4.2. Characteristics of Deep and Bottom Waters

Upper Circumpolar Deep Water (UCDW) is best characterized by the presence of subsurface temperature maximum T_{max} or oxygen minimum O_{2min}. T_{max} is formed as the consequence of T_{min} thus can be observed to the south of the PF, with its values in the UFZ region varying between 2.5 °C at the PF and 2 °C at the SB. Therefore, in the UFZ region, T_{max} less than 2 °C is not observed within the ACC band. At the SACCF in the A section, T_{max} is 2.2 °C, and corresponding T_{min} is close to 0 °C (see Figures 8a and 9a), verifying once again that the 0 °C T_{min} and the 1.8 °C T_{max} (Orsi et al., 1995) should not be used together as the dual hydrographic criteria of the SACCF, as already mentioned. A plausible explanation for this precautionary statement may be that the 1.8 °C UCDW observed at the SACCF at the Greenwich Meridian by Orsi et al. (1995) might have already traversed the ACC band to extend poleward into the subpolar regime while flowing in the downstream regions. This evidence of the cross-frontal poleward flow of UCDW is consistent with Tamsitt et al. (2017) who tracked poleward spiraling/upwelling pathways of global deep waters to the surface of the

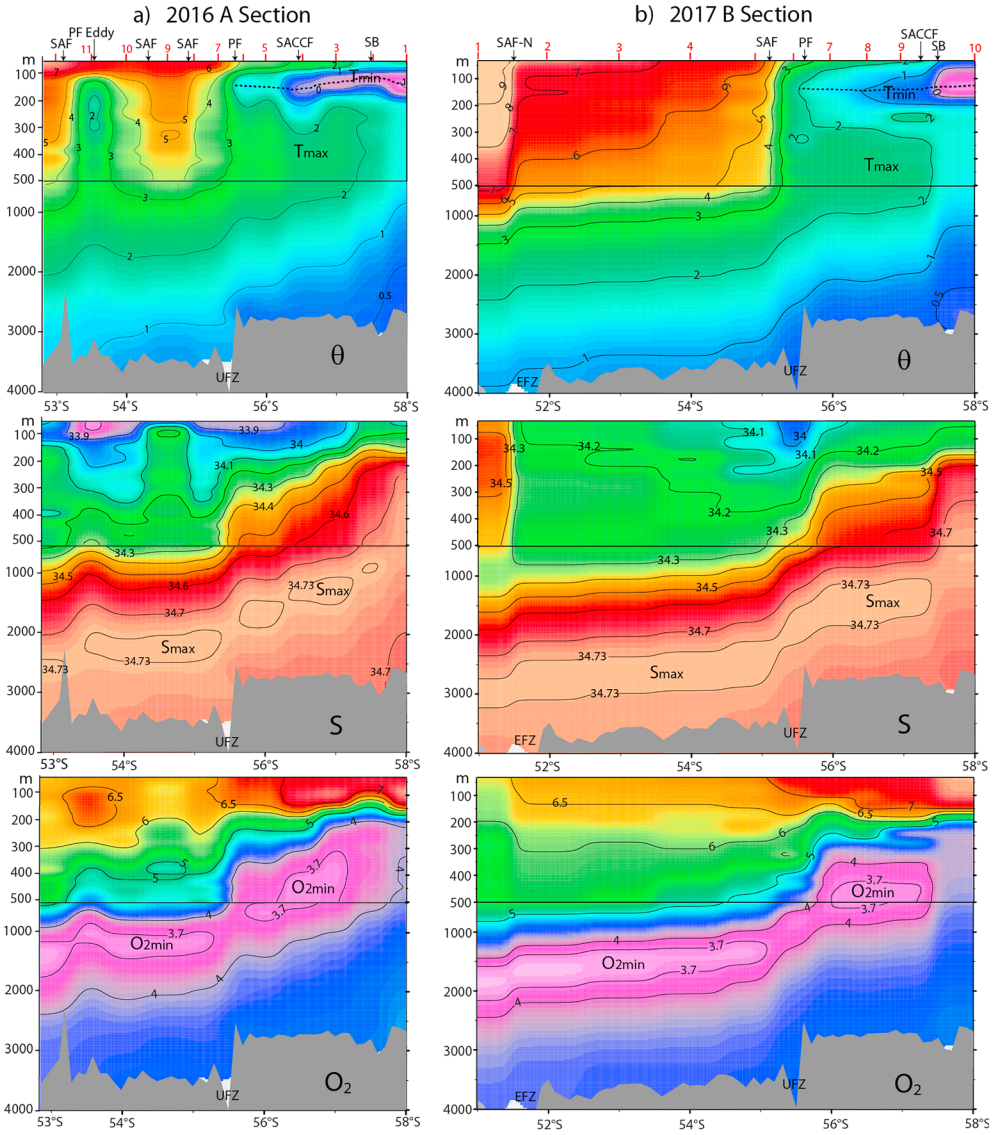

Figure 8. Property sections from (a) the 2016 A section and (b) the 2017 B section. Units are degrees Celsius for potential temperature θ, unitless Practical Salinity S, and milliliters per liter for oxygen content O_2. Locations of the hydrography-derived Antarctic Circumpolar Current fronts discussed in the text are indicated beside station numbers (red) on top of the temperature sections. SAF = Subantarctic Front; PF = Polar Front; SACCF = Southern Antarctic Circumpolar Current Front; SB = southern boundary; UFZ = Udintsev Fracture Zone; SAF-N = northern SAF; EFZ = Eltanin Fracture Zone.

Southern Ocean in high-resolution models. $O_{2\text{min}}$, which represents the influence of the least ventilated deep waters of Pacific and Indian origins (Callahan, 1972; Park et al., 1993), shows in the UFZ region a modal characteristic at θ = 2.5 °C, O_2 = 3.6 ml/L (Figures 9c and 9d), corresponding to a minimum oxygen saturation (about 50%) of the region.

Lower Circumpolar Deep Water is best characterized with the presence of a subsurface salinity maximum S_{max} originating from the North Atlantic, which in the UFZ region is saltier than 34.73 except at the southernmost station outside of the ACC where S_{max} becomes slightly fresher and colder (Figure 8). Finally, it is interesting to note that no bottom water colder than 0.2 °C is found in the UFZ region; bottom water temperature there varies between 0.23 and 1.08 °C, with the coldest bottom water within the ACC band being ~0.5 °C at the SB. The coldest bottom water at the southernmost station (0.23 °C) has a neutral density γ_n ~ 28.25 kg/m^3, which is slightly lighter than the upper limit (γ_n = 28.27 kg/m^3) of the conventional Antarctic Bottom Water (Orsi et al., 1999). As the last ACC choke point before arriving at Drake Passage,

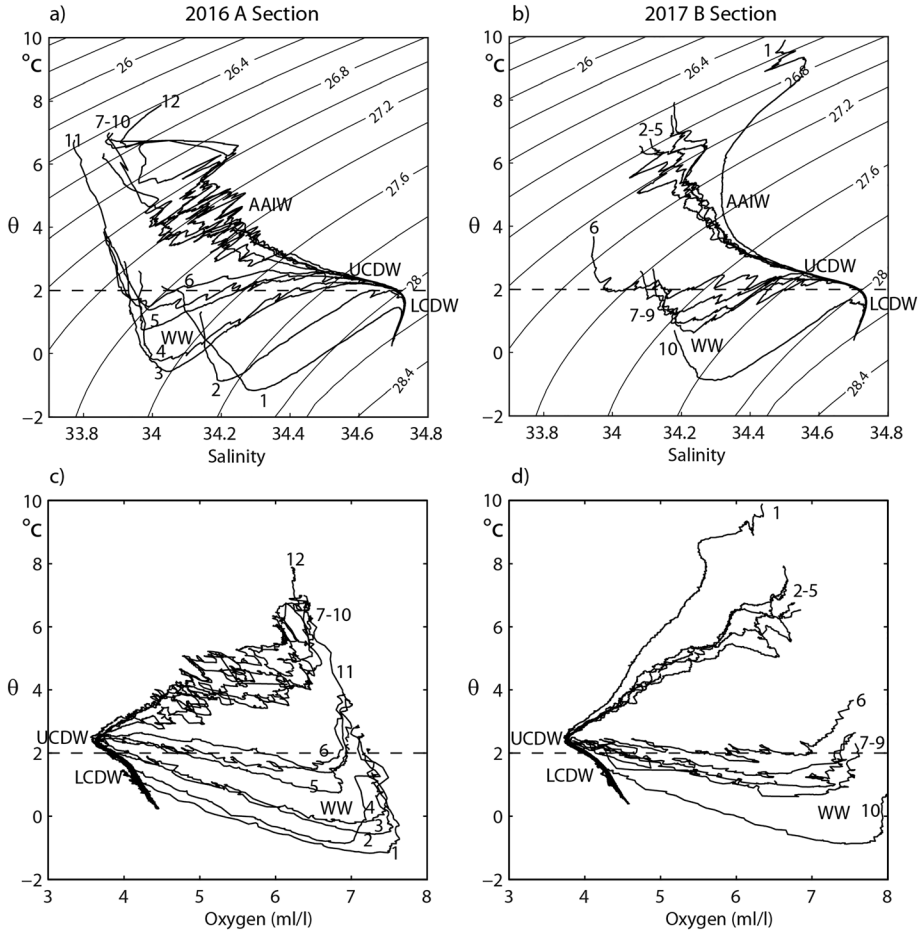

Figure 9. θ -S and θ -O_2 diagrams for (a, c) the 2016 A section and (b, d) the 2017 B section. The Arabic numerals beside property-property correlation curves designate station numbers. Neutral density isolines are inserted in (a) and (b). The dashed horizontal lines correspond to $\theta = 2$ °C, the northern limit of Winter Water (WW). Major water masses discussed in the text are also indicated. AAIW = Antarctic Intermediate Water; UCDW = Upper Circumpolar Deep Water; LCDW = Lower Circumpolar Deep Water.

the observed deep and bottom water characteristics in the UFZ region should serve as a useful reference for interpreting any downstream modifications of these water masses before they reach Drake Passage.

4.3. Geostrophic Velocities and Transport

Across-section geostrophic velocities and transport are estimated relative to the deepest common depths between adjacent station pairs (Figure 10). In the A section (Figure 10a), we observe two deep-reaching bands of strong flow with a peak surface velocity >0.5 m/s, which are centered at 55°25′S in between the closely located PF and SAF as well as at 53°15′S corresponding to the northernmost SAF location associated with its S-shape meander. The westward meandering branch of SAF can be seen at 53°45′S by a deep-reaching westward flow with a peak surface velocity of −0.2 m/s. Aside from this strong westward flow associated with the SAF meandering circulation, the central jet at 55°25′S is also associated on its northern and southern flanks with a sluggish westward flow, suggesting the presence of prominent mesoscale eddy activity during the occupation of the A section. This is confirmed by the altimetry-derived sea level anomaly and surface velocity fields (Figure 11) showing highly perturbed fields during the 2016 cruise period (Figure 11a), with the presence of a well-developed cyclonic eddy centered at 53°30′S, 141°40′W. In addition, there are in Figure 10a two bands of secondary eastward flow (<0.15 m/s) at 56°15′S and 57°30′S close to the SACCF and the SB, respectively.

Across the A section, transport of O(30–35 Sv) (1 Sv = 10^6 m^3/s) is estimated for each of the above two major eastward jets associated with the combined SAF/PF and the S-shape meandering SAF, while much smaller

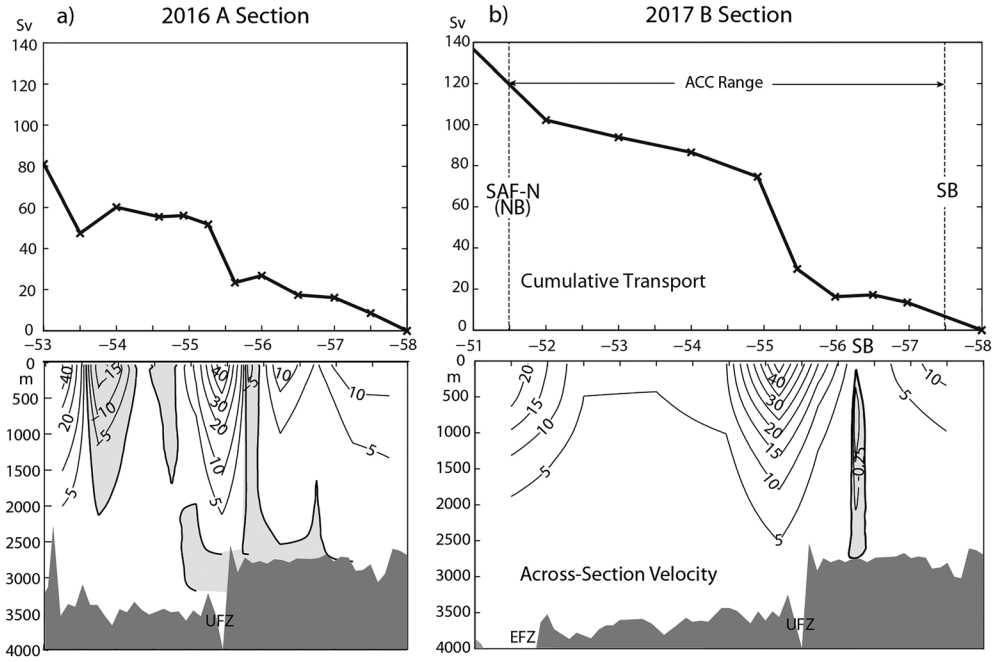

Figure 10. Vertical sections of velocity (lower panels, cm/s) perpendicular to (a) the 2016 A section and (b) the 2017 B section, with corresponding cumulative transports from the south (upper panels, Sv). Westward flow is lightly shaded. SAF-N = northern Subantarctic Front; NB = northern boundary; SB = southern boundary; ACC = Antarctic Circumpolar Current; EFZ = Eltanin Fracture Zone; UFZ = Udintsev Fracture Zone.

transport of *O*(10 Sv) for the two secondary jets associated with the SACCF and SB. Net transport across the entire section amounts to 81 Sv, which is much smaller compared to the baroclinic transport component of 112 Sv at Drake Passage (Koenig et al., 2016). This is not surprising as the A section does not cut the entire ACC breadth but misses its northern limb, as already mentioned.

In the B section (Figure 10b), in contrast, we observe a much simpler three-band frontal structure of eastward flow, without any prominent mesoscale feature, which is also consistent with the altimetry-derived flow field (Figure 11b) showing a featureless sluggish flow between 52°S and 55°S. A deep-reaching central jet with a peak surface velocity of ~0.5 m/s centered at 55°15′S is widely developed between 54°30′S and 56°S through the combined SAF/PF in the UFZ. Other two prominent bands of eastward flow are found near the SAF-N and SB with a moderate peak velocity <0.15–0.2 m/s, which are well separated from the central jet by a sluggish flow <0.05–0.1 m/s.

Transports associated with the above three jets across the B section are approximately 75 Sv for the central jet, 35 Sv for the northernmost jet, and 15 Sv for the southernmost jet, while the net transport across the

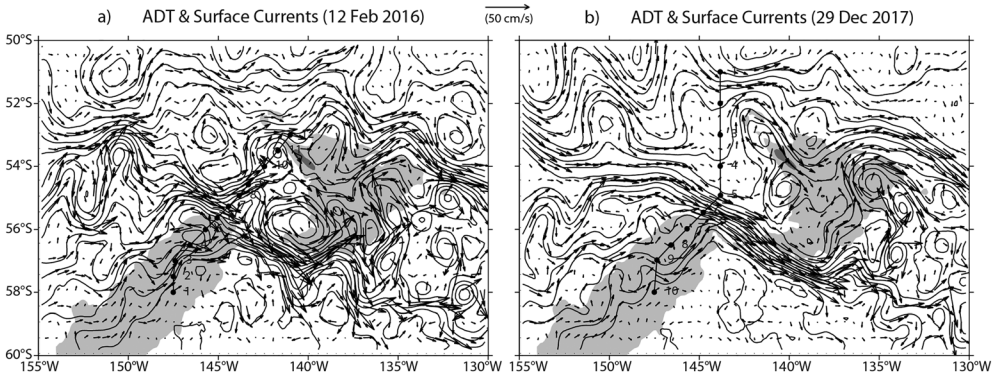

Figure 11. Snapshots of absolute dynamic topography (ADT, contours every 0.2 m) and surface velocities (arrows, scale at the top center) for the central day of (a) the 2016 cruise and (b) the 2017 cruise.

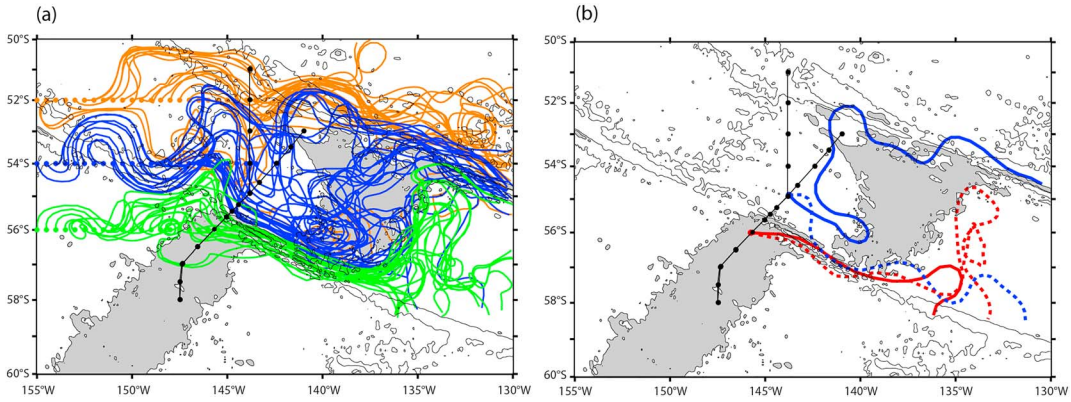

Figure 12. Trajectories of synthetic particles in the study area forward tracked for 6 months (November 2015 to April 2016) using the high-resolution altimetric velocity time series fields. Initial positions of particles are indicated by dots along three latitudes (52°, 54°, and 56°S) west of 144°W, mimicking the northern boundary (orange), Subantarctic Front (blue), and Polar Front (green). (a) Entire trajectories tracked from all initial positions. (b) Selected two pairs of trajectories starting from the climatological Subantarctic Front (solid blue line) and Polar Front (solid red line) locations on the cruise sections and those a month apart (dotted lines). Isobaths 3,000 and 4,000 m are shown, with depths shallower than 3,000 m being shaded.

entire section is 138 Sv. As we have defined the SAF-N (or NB) at a halfway between the two northernmost stations, we attribute one half of the northernmost transport to the ACC and the other half to the subtropical regime outside of the ACC. Similarly, we attribute one half of the southernmost transport to the ACC and the other half to the subpolar regime outside of the ACC. Consequently, the net baroclinic transport of the ACC across the B section amounts to 113 Sv relative to the bottom, which coincides fortuitously with that through Drake Passage of 112 Sv estimated by Koenig et al. (2016). About 60% of this transport is concentrated at the entrance of the UFZ where the SAF and PF are tightly combined within a narrow latitudinal range of 1.5° between 54°30′S and 56°S.

Finally, we would like to briefly mention the order of magnitude of bottom velocities and corresponding barotropic component of transport from preliminary analysis of the recovered current meter data. In fact, the record length-mean value at the northern (southern) mooring site at 55°S (57°S) has a bottom velocity perpendicular to the section of 0.029 (0.048) m/s (the central mooring at 56°S could not be recovered). Assuming that these time-mean bottom velocities are representative for the 1.5°-wide central jet (54°30′–56°S) and the 0.5°-wide southern jet associated with the SB (57°–57°30′S) and multiplying the vertical area of each jet segment, we roughly estimate a total barotropic transport across the section of about 25 Sv. This value is the same order of magnitude as the 28-Sv barotropic transport component at Drake Passage (Koenig et al., 2016), although the agreement may be highly fortuitous given the very rough approximations used for our transport estimation. The total ACC transport through the UFZ region amounts then to 138 Sv, which is also nearly same as that through Drake Passage (140 Sv) by Koenig et al. (2016). However, the conclusion does not change with a canonical value of 134 Sv according to Whitworth and Peterson (1985), except for a 30% higher estimate of 173 Sv by Donohue et al. (2016). The key point here is not the exact value inaccessible from our limited observations but rather resides in the order of magnitude of the relative importance of the barotropic component of ACC transport compared to its total transport, which is roughly 20% in the UFZ region, in agreement with Koenig et al. (2016) at Drake Passage.

5. Spatiotemporal Variability of the Frontal Circulation in the UFZ Region

5.1. Trajectories of Synthetic Particles From Altimetry

Lagrangian trajectories of synthetic particles are tracked in the UFZ region (Figure 12) using the fine-resolution (1-day temporal resolution and 1/8° spatial resolution) altimetric velocity time series specially prepared for our study, as mentioned in section 2.2. Note that daily absolute velocities used here are the sum of the 1/8°-resolution velocity anomalies and the CNES_CLS18 MDT. We have used a simple prediction-correction scheme similar to that employed by Filippi et al. (2010), which has been successfully applied in the Kerguelen region (Park et al., 2014). Synthetic particles are seeded at intervals of 0.1° in

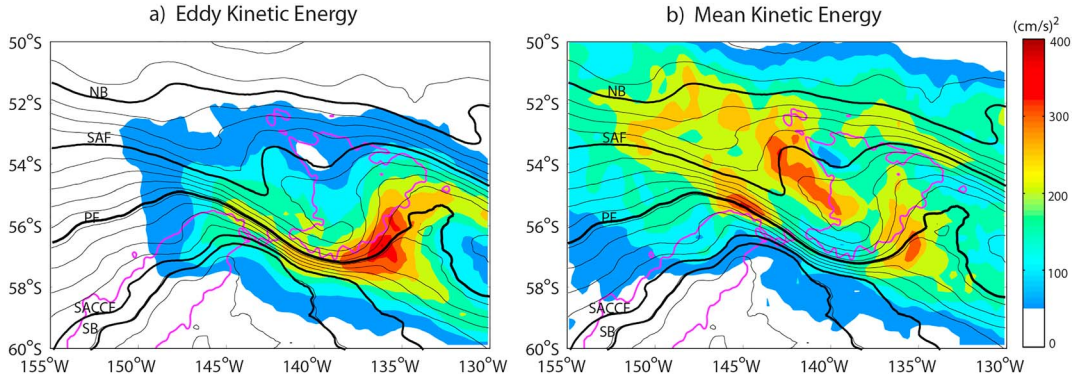

Figure 13. Maps showing (a) the eddy kinetic energy and (b) the mean kinetic energy in square centimeters per square second averaged over 1993–2018. The 3,000-m isobath is shown in magenta. Other comments are same as in Figure 2.

longitude between 144° and 155°W along three selected latitudes 52°, 54°, and 56°S (Figure 12a). Different colors attributed to different initial latitudes are intended to follow those particles that are roughly associated with different fronts: orange for the NB, blue for the SAF, and green for the PF. We remark in this map a mixture of different flow patterns such as a simple sinusoidal meander of SAF in the area west of 144°W, a straight downstream flow of the PF through the UFZ and that of the SAF through the EFZ, irregularly evolving S-shape meandering of SAF in the immediate upstream area of the offset PAR segment, and northward deflection of the northern branch of the PF along the eastern flank of the offset PAR segment. There appears a great similitude between the envelopes of different colors (or fronts) and the climatological mean locations of the ACC fronts from both altimetry and hydrography (see Figures 2 and 7).

The SAF does not cross directly the relatively shallow offset PAR segment but often describes an abrupt westward retroflection on impinging on the western flank of the latter ridge segment and turns northward before flowing eastward through the EFZ. Therefore, the most complex pattern of trajectories with an occasional extreme meridional excursion over 400–500 km is observed around the offset PAR segment. An example of this feature is shown in Figure 12b which shows two pairs of trajectories separated in time by 1 month (solid and dotted lines) which are launched from two different points corresponding to the climatological locations of the SAF (blue lines) and the PF (red lines). Note that the blue solid line starting from the climatological location of the SAF shows first a southeastward flow before making a complete westward retroflection on impinging on the southwestern flank of the offset PAR segment and then meandering northward to pass through the EFZ. The blue dotted line, which has started from the same SAF location but 1 month apart, bends southward to join the flow channeling through the UFZ, thus completely separating from the blue solid line by up to 4° in latitude. The two red trajectories starting from the same PF location show first a similar flow through the UFZ until 137°W, where the solid one makes a clockwise turning to the south, whereas the dotted one makes an anticlockwise turning to the north before performing a meridionally elongated looping over 3° in latitude in the east of the offset PAR segment. Thus, Figure 12b clearly demonstrates the occasional extreme changes of particle trajectories around the offset PAR segment, which is likely associated with changing polarity of local mesoscale features. In summary, the complex regional ridge system composed of the PAR, the offset PAR segment, the UFZ, and the EFZ thus exerts a crucial topographic control on the regional circulation by favoring a tight convergence of the three major ACC fronts at the entrance of the UFZ at 144°W. In addition, the presence of the relatively shallow offset PAR segment diverts the SAF northward to pass through the EFZ, completely separating the SAF from the PF by about 4° in latitude at the exit of the UFZ at 137°W.

5.2. EKE From Altimetry

Time-averaged eddy kinetic energy (EKE) is calculated as ½ ($u^2 + v^2$) from 25 years of altimetry-derived daily geostrophic velocity data (u, v) which have previously been high-pass filtered with a 90-day cutoff (Figure 13a). This cutoff period first employed by Nowlin et al. (1985) is intended to isolate mesoscale fluctuations of currents from their slowly varying components associated with lateral shifts of the frontal structure or meandering flow. The highest EKE up to O(400 cm^2/s^2) is centered at (57°S, 136°W) at the outlet of

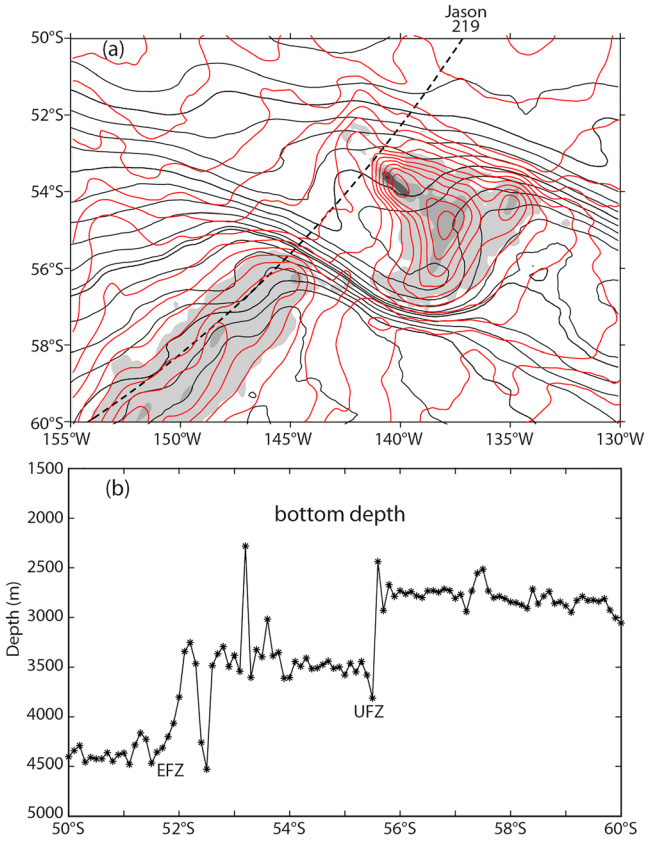

Figure 14. (a) Geostrophic contours f/h (red, C.I. = 2×10^{-9} s^{-1} m^{-1}) superposed on Mean Dynamic Topography contours (black, C.I. = 0.1 m). (b) The quasi-meridional profile of bathymetry along the Jason ground track 219 shown in (a). EFZ = Eltanin Fracture Zone; UFZ = Udintsev Fracture Zone.

UFZ southeast of the offset PAR segment. Elevated EKE >200 cm^2/s^2 is found along the PF and its vicinity, with the most prominent EKE (>300 cm^2/s^2) being found not within the strongest jet axis but in a weak flow regime associated with the northward diverging PF from the SACCF near the southeastern corner of the offset PAR segment. In the area to the north of the SAF and to the south of the SACCF, we observe very weak EKE (<100 cm^2/s^2), with a negligible value (<50 cm^2/s^2) outside of the ACC band and to the west of 150°W. It is interesting to remark that the high EKE is not associated with the strong jet of SAF nor with its S-shape meandering in the area immediate upstream of the offset PAR segment. By correlating with corresponding temperature anomalies, mesoscale eddy velocities may yield poleward heat fluxes (e.g., Nowlin et al., 1985), and it remains to see whether the regional hot spot of poleward eddy heat flux coincides precisely with the PF divergence area showing the highest EKE, which is left for a future investigation.

To complete the discussion, we show in Figure 13b the low-frequency MKE computed from the daily geostrophic velocity data low-pass filtered with a 90-day cutoff, which should represent the kinetic energy associated with the slowly varying mean flow. The significant MKE is more widely distributed and dominates the EKE in the area upstream of the offset PAR segment, with two poles centered at the UFZ at 144°W and the S-shape meandering SAF. Downstream of the offset PAR segment, on the contrary, the EKE largely dominates the MKE especially around the northward diverging PF. Figure 13 thus illustrates a clear regional contrast between the mean flow-dominated and eddy flow-dominated regimes.

6. Discussion

In this study an up-to-date map of the ACC fronts is constructed from the latest version of satellite altimetry, enabling us to ascertain that the UFZ region at 144°W appears as the narrowest choke point of the entire circumpolar longitudes. Here the three major ACC fronts are most strongly confluent within a limited latitudinal range as short as 1.5° in latitude, which is ~40% narrower than that in Drake Passage. In situ observations from our two recent cruises in the UFZ region well confirm the altimetry-derived frontal circulation of the region. Consistent with the altimetry-derived ACC fronts, the ACC transport estimated from the cruise data is also strongly concentrated at the UFZ choke point, with a bottom-referenced baroclinic transport of 113 Sv (with a very rough estimate of the total ACC transport of 138 Sv), well consistent with estimates at Drake Passage.

How can we explain the strongest concentration of the ACC in the UFZ which is devoid of any nearby continental boundaries constraining the meridional extent of the circumpolar flow such as in Drake Passage? The answer can be found in the bottom topography along the Jason altimeter track 219 (Figure 14b), which reveals a staircase step-like bathymetric jump by about 1,000 m across the fault zones of the EFZ at 52°S and the UFZ at 55°30′S. Such a near-vertical wall of 1,000-m height should quasi-permanently support the near-bottom pressure gradient force exerted by an overlying bottom-reaching eastward jet, which may explain the observed two well-distinguished permanent jets (SAF and PF) anchoring at each fracture zone. In addition, the geographical configuration of the ridge system especially the lateral shift in ridge axis between the PAR and the offset PAR segment, which actually forms the UFZ, makes the entrance of the UFZ over the northern escarpment of the PAR at 144°W a privileged convergence zone of the three major ACC fronts. The relatively shallow topography of the offset PAR segment acts as an obstacle to the eastward progression of the SAF, which meanders rather northward before channeling through the EFZ.

Alternatively, the above topographic steering can be explained by the conservation of potential vorticity (f/h, neglecting relative vorticity, where f is the Coriolis parameter and h is bottom depth) of the depth averaged

flow. In effect, geostrophic contours f/h (red contours in Figure 14a) round the PAR and offset PAR segment, with their strongest concentration in the UFZ and EFZ, roughly parallel at places with MDT contours (black). Geostrophic contours also show evidence of S-shape meandering upstream of the offset PAR segment. This illustrates example of how the ACC negotiates the fracture zones presenting a steep bottom slope.

Finally, deep water characteristics identified in the UFZ region should provide an invaluable reference for adequately interpreting downstream modifications of deep and bottom waters before they reach Drake Passage. As the prime choke point of the ACC, the UFZ can thus be used in the future as an additional reference site supplementing Drake Passage for investigating the ACC dynamics and modifications of water masses characteristics in relation to the Southern Ocean meridional overturning circulation. Any upstream/downstream changes in deep and bottom waters in the other sectors should be related to the Southern Ocean meridional overturning circulation. Moreover, the flow-topography interaction appears as the prime factor controlling the local ACC dynamics in the UFZ region. In this sense, the UFZ region provides a crucial site for monitoring the ACC transport and its temporal variability as well as for estimating the local poleward heat flux. The mean-flow contribution to the latter flux (e.g., Sekma et al., 2013) may presumably be best estimated at the entrance of the UFZ at 144°W, whereas its eddy contribution at the outlet of the UFZ at 136°W where the highest EKE is observed. Any institution/nation having an Antarctic supply ship navigating regularly in the same sector might find the UFZ region scientifically interesting (and economically too due to its narrowness) for long-term monitoring of the ACC, for which our results presented here are hopefully useful and encouraging.

Acknowledgments
The program PHANTOM of LOCEAN/Sorbonne University is partly supported by CNES, with a technical support of Institut National des Sciences de l'Univers, Brest, for preparing mooring instruments. T. P., T. W. K., and S. H. L. are supported by the Korea Polar Research Institute grant KOPRI PE18060. C. S. H. and J. H. L. are supported by KOPRI through KIOST PN66500. We are grateful to KOPRI for the ship time to access this remote location and to the Captain and crew of Araon for their devoted professional efforts. Valuable comments from Igor Belkin and an anonymous reviewer helped us improve the original manuscript in clarifying the hydrographic criteria of the NB, the newly defined northernmost ACC front from altimetry. The CTD/O_2 data used are in public archives SEANOE: CTDO Sections at the Udintsev Fracture Zone (https://doi.org/10.17882/59853). The geographical coordinates of the altimetry-derived five ACC fronts are also in public archives SEANOE: Altimetry-derived Antarctic Circumpolar Current fronts (https://doi.org/10.17882/59800).

References

Abernathey, R., & Cessi, P. (2014). Topographic enhancement of eddy efficiency in baroclinic equilibration. *Journal of Physical Oceanography*, *44*(8), 2107–2126. https://doi.org/10.1175/JPO-D-14-0014.1

Artana, C., Ferrari, R., Koenig, Z., Saraceno, M., Piola, A. R., & Provost, C. (2016). Malvinas Current variability from Argo floats and satellite altimetry. *Journal of Geophysical Research: Oceans*, *121*, 4854–4872. https://doi.org/10.1002/2016JC011889

Barré, N., Provost, C., Renault, A., & Sennéchael, N. (2011). Fronts, meanders and eddies in Drake Passage during the ANT-XXIII/3 cruise in January–February 2006: A satellite perspective. *Deep Sea Research Part II: Topical Studies in Oceanography*, *58*(25), 2533–2554. https://doi.org/10.1016/j.dsr2.2011.01.003

Belkin, I. M., & Gordon, A. L. (1996). Southern Ocean fronts from the Greenwich meridian to Tasmania. *Journal of Geophysical Research*, *101*, 3675–3696. https://doi.org/10.1029/95JC02750

Botnikov, V. N. (1963). Geographical position of the Antarctic convergence zone in the Pacific Ocean. *Soviet Antarctic Expedition Information Bulletin English Translation*, *4*, 324–327.

Callahan, J. E. (1972). The structure and circulation of deep water in the Antarctic. *Deep Sea Research*, *19*, 563–575.

Donohue, K. A., L, K., Watts, D. R., Chidichimo, M. P., & Chereskin, T. K. (2016). Mean Antarctic Circumpolar Current transport measured in Drake Passage. *Geophysical Research Letters*, *43*, 11,760–11,767. https://doi.org/10.1002/2016GL070319

Fecher, T., Pail, R., & Gruber, T. (2017). GOCO05c: A new combined gravity field model based on full normal equations and regionally varying weighting. *Surveys in Geophysics*, *38*(3), 571–590. https://doi.org/10.1007/s10712-016-9406-y

Filippi, J.-B., Komatsu, T., & Tanaka, K. (2010). Simulation of drifting seaweeds in East China Sea. *Ecological Informatics*, *5*, 67–72.

Gille, S. T. (1999). Mass, heat, and salt transport in the southeastern Pacific: A circumpolar current inverse model. *Journal of Geophysical Research*, *104*, 5191–5209.

Hoskins, B. J., James, I. N., & White, G. H. (1983). The shape, propagation and mean-flow interactions of large-scale weather systems. *Journal of the Atmospheric Sciences*, *40*(7), 1595–1612. https://doi.org/10.1175/1520-0469(1983)040<1595:TSPAMF>2.0.CO;2

Hughes, C. W., & Ash, E. R. (2001). Eddy forcing of the mean flow in the Southern Ocean. *Journal of Geophysical Research*, *106*, 2713–2722.

Kim, Y.-S., & Orsi, A. H. (2014). On the variability of Antarctic Circumpolar Current fronts inferred from 1992-2011 altimetry. *Journal of Physical Oceanography*, *44*(12), 3054–3071. https://doi.org/10.1175/JPO-D-13-0217.1

Koenig, Z., Provost, C., Park, Y.-H., Ferrari, R., & Sennéchael, N. (2016). Anatomy of the Antarctic Circumpolar Current volume transports through Drake Passage. *Journal of Geophysical Research: Oceans*, *121*, 2572–2595. https://doi.org/10.1002/2015JC011436

Meredith, M. P., Watkins, J. L., Murphy, E. J., Ward, P., Bone, D. G., Thorpe, S. E., et al. (2003). Southern ACC Front to the northeast of South Georgia: Pathways, characteristics, and fluxes. *Journal of Geophysical Research*, *108*(C5), 3162. https://doi.org/10.1029/2001JC001227

Nowlin, W. D. Jr., Whitworth, T. III, & Pillsbury, R. B. (1977). Structure and transport of the Antarctic Circumpolar Current at Drake Passage from short-term measurements. *Journal of Physical Oceanography*, *7*, 788–802.

Nowlin, W. D. Jr., Worley, S. J., & Whitworth, T. III (1985). Methods for making point estimates of eddy heat flux as applied to the Antarctic Circumpolar Current. *Journal of Geophysical Research*, *90*(C2), 3305–3324. https://doi.org/10.1029/JC090iC02p03305

Orsi, A. H., Johnson, G. C., & Bullister, J. L. (1999). Circulation, mixing, and production of Antarctic Bottom Water. *Progress in Oceanography*, *43*, 55–109.

Orsi, A. H., Whitworth, T. III, & Nowlin, W. D. Jr. (1995). On the meridional extent of the Antarctic Circumpolar Current. *Deep-Sea Research Part I*, *42*, 641–673. https://doi.org/10.1016/0967-0637(95)00021-W

Park, Y.-H., Charriaud, E., Craneguy, P., & Kartavtseff, A. (2001). Front, transport, and Weddell Gyre at 30°E between Africa and Antarctica. *Journal of Geophysical Research*, *106*, 2857–2879.

Park, Y.-H., Durand, I., Kestenare, E., Rougier, G., Zhou, M., d'Ovidio, F., et al. (2014). Polar Front around the Kerguelen Islands: An up-to-date determination and associated circulation of surface/subsurface waters. *Journal of Geophysical Research: Oceans*, *119*, 6575–6592. https://doi.org/10.1002/2014JC010061

Park, Y.-H., Gambéroni, L., & Charriaud, E. (1993). Frontal structure, water masses and circulation in the Crozet Basin. *Journal of Geophysical Research*, *98*, 12,361–12,385. https://doi.org/10.1029/93JC00938

Park, Y.-H., Vivier, F., Roquet, F., & Kestenare, E. (2009). Direct observations of the ACC transport across the Kerguelen Plateau. *Geophysical Research Letters*, *36*, L18603. https://doi.org/10.1029/2009GL039617

Pollard, R. T., Venables, H. J., Read, J. F., & Allen, J. T. (2007). Large-scale circulation around the Crozet Plateau controls an annual phytoplankton bloom in the Crozet Basin. *Deep-Sea Research Part II*, *54*, 1915–1929.

Provost, C., Renault, A., Barré, N., Sennéchael, N., Garçon, V., Sudre, J., & Huhn, O. (2011). Two repeat crossings of Drake Passage in austral summer 2006: Short-term variations and evidence for considerable ventilation of intermediate and deep waters. *Deep-Sea Research Part II*, *58*, 2555–2571.

Pujol, M.-I., Schaeffer, P., Faugère, Y., Raynal, M., Dibarboure, G., & Picot, M. (2018). Gauging the improvement of recent mean sea surface models: A new approach for identifying and quantifying their errors. *Journal of Geophysical Research: Oceans*, *123*, 5889–5911. https://doi.org/10.1029/2017JC013503

Rio, M. H., Guinehut, S., & Larnicol, G. (2011). New CNES-CLS09 global mean dynamic topography computed from the combination of GRACE data, altimetry, and in situ measurements. *Journal of Geophysical Research*, *116*, C07018. https://doi.org/10.1029/2010JC006505

Rio, M.-H., Mulet, S., & Picot, N. (2014). Beyond GOCE for the ocean circulation estimate: Synergetic use of altimetry, gravimetry, and in situ data provides new insight into geostrophic and Ekman currents. *Geophysical Research Letters*, *41*, 8918–8925. https://doi.org/10.1002/2014GL061773

Roquet, F., Park, Y.-H., Guinet, C., Bailleul, F., & Charrassin, J.-B. (2009). Observations of the Fawn Trough Current over the Kerguelen Plateau from instrumented elephant seals. *Journal of Marine Systems*, *78*(3), 377–393. https://doi.org/10.1016/j.jmarsys.2008.11.017

Sekma, H., Park, Y.-H., & Vivier, F. (2013). Time-mean flow as prevailing contribution to the poleward heat flux across the southern flank of the Antarctic Circumpolar Current: A case study in the Fawn Trough, Kerguelen Plateau. *Journal of Physical Oceanography*, *43*, 583–601. https://doi.org/10.1175/JPO-D-12-0125.1

Sokolov, S., & Rintoul, S. R. (2002). Structure of Southern Ocean fronts at 140°E. *Journal of Marine Systems*, *37*(1-3), 151–184. https://doi.org/10.1016/S0924-7963(02)00200-2

Sokolov, S., & Rintoul, S. R. (2009). Circumpolar structure and distribution of the Antarctic Circumpolar current fronts: 1. Mean circumpolar paths. *Journal of Geophysical Research*, *114*, C11019. https://doi.org/10.1029/2008JC005108

Tamsitt, V. H., Drake, H. F., Morrison, A. K., Talley, L. D., Dufour, C. O., Gray, A. R., et al. (2017). Spiraling pathways of global deep waters to the surface of the Southern Ocean. *Nature Communications*, *8*, 172. https://doi.org/10.1038/s41467-00197-0

Thompson, A. F., & Sallée, J.-B. (2012). Jets and topography: Jet transitions and the impact on transport in the Antarctic Circumpolar Current. *Journal of Physical Oceanography*, *42*, 956–972. https://doi.org/10.1175/JPO-D-11-0135.1

Thompson, A. F., Stewart, A. L., Spence, P., & Heywood, K. J. (2018). The Antarctic Slope Current in a changing climate. *Reviews of Geophysics*, *56*, 741–770. https://doi.org/10.1029/2018RG000624

Taburet, G., Sanchez-Roman, A.,Ballarotta, M., Pujol, M. -I, Legeais, J.-F., Fournier, F., Faugere, Y., & Dibarboure, G..(2019). DUACS DT-2018: 25 years of reprocessed sea level altimeter products. *Ocean Sci. Discuss*, *44*(8), 2107–2126. https://doi.org/10.5194/os-2018-150

Ubelmann, C., Klein, P., & Fu, L. L. (2015). Dynamic interpolation of sea surface height and potential applications for future high-resolution altimetry mapping. *Journal of Atmospheric and Oceanic Technology*. https://doi.org/10.1175/JTECH-D-14-00152.1

Vlastélic, I., & Dosso, L. (2005). Initiation of a plume-ridge interaction in the South Pacific recorded by high-precision Pb isotopes along Hollister Ridge. *Geochemistry, Geophysics, Geosystems*, *6*, Q05011. https://doi.org/10.1029/2004GC000902

Whitworth, T. III, & Nowlin, W. D. Jr. (1987). Water masses and currents of the Southern Ocean at the Greenwich Meridian. *Journal of Geophysical Research*, *92*, 6462–6476.

Whitworth, T., & Peterson, R. (1985). Volume transport of the Antarctic Circumpolar Current from bottom pressure measurements. *Journal of Physical Oceanography*, *15*, 810–816.

Williams, R. G., Wilson, C., & Hughes, C. W. (2007). Ocean and atmosphere storm tracks: The role of eddy vorticity forcing. *Journal of Physical Oceanography*, *37*, 2267–2289. https://doi.org/10.1175/JPO3120.1